https://doi.org/10.5194/tc-2021-343
Preprint. Discussion started: 29 November 2021

The Cryosphere Discussions

The effect of changing sea ice on nearshore wave climate trends along Alaska's central Beaufort Sea coast

Kees Nederhoff[1], Li Erikson[2], Anita Engelstad[2], Peter Bieniek[3], Jeremy Kasper[4]

[1] Deltares USA, 8601 Georgia Ave., Silver Spring, MD 20910, USA
[2] U.S. Geological Survey Pacific Coastal and Marine Science Center, 2885 Mission St., Santa Cruz, CA 95060, USA
[3] International Arctic Research Center, University of Alaska, Fairbanks, PO Box 757340, Fairbanks, AK 99775-7340, USA
[4] Alaska Center for Energy and Power, University of Alaska Fairbanks, Fairbanks, AK 99775, USA

Correspondence to: Kees Nederhoff (kees.nederhoff@deltares-usa.us)

Abstract. Diminishing sea ice is impacting the wave field across the Arctic region. Recent observation and model-based studies highlight the spatiotemporal influence of sea ice on offshore wave climatologies, but effects within the nearshore region are still poorly described. This study characterizes the wave climate in the central Beaufort Sea coast from 1979 to 2019 by utilizing a wave hindcast model that uses ERA5 winds, waves, and ice concentrations as input. The spectral wave model SWAN is calibrated and validated based on more than 10,000 *in situ* measurements collected over a 13-year time period across the region, with friction variations and empirical coefficients for newly implemented empirical ice formulations for the open water season. Model results and trends are analyzed over the 41-year time period using the non-parametric Mann-Kendall test, including an estimate of Sen's slope. The model results show that the reduction of sea ice concentration correlates strongly with increases in average and extreme wave conditions. In particular, the open water season extended by ~96 days over the 41-year time period (~2.4 days/yr), resulting in a five-fold increase of the yearly cumulative wave power. Moreover, the open water season extends later into the year, resulting in relatively open-water conditions during fall storms with high wind speeds. The later freeze-up results in an increase of the annual offshore median wave heights of 1% per year and an increase in the average number of rough wave days (defined as days when maximum wave heights exceed 2.5 m) from 1.5 in 1979 to 13.1 days in 2019. Trends in the nearshore areas deviate from the patterns offshore. Model results indicate a non-breaking depth-induced saturation limit for high wave heights in the shallow areas of Foggy Island Bay. Similar patterns are found for yearly cumulative wave power.

1 Introduction

Receding Arctic Ocean ice coverage is increasing commercial opportunities such as shipping of goods and oil and gas interests along the shores of Alaska's north coast (O'Rourke, 2020; Perrie, 2013; Aksenov, 2017). However, rising air and ocean temperatures are changing the climate regime (Navarro et al., 2016; Overland et al., 2016), and may pose new challenges to commercial activities in the region. Additional oceanographic data will improve the understanding of how future changes will affect wave climatology and its impact on existing and planned infrastructure. Coastal arctic activities and marine infrastructure will be susceptible to disruption, decay, and catastrophic failure if wind-wave energy increases, if swell waves emerge along the

https://doi.org/10.5194/tc-2021-343
Preprint. Discussion started: 29 November 2021

otherwise fetch-limited Alaska Arctic coast, and if storm surge levels increase (Erikson et al., 2015; Pisaric et al., 2011; Thomson et al., 2016; Thomson and Rogers, 2014).

Recent interest and advancements in satellite technology, processing techniques, and modeling have resulted in several new studies that highlight and illuminate the effects of increasing median and extreme wave conditions across the Arctic Ocean (Casas-Prat et al., 2018; Casas-Prat and Wang, 2020; Liu et al., 2016; Stopa et al., 2016; Francis et al., 2011). Few studies, however, can resolve changes within the nearshore region, here defined as the portion of the shelf between the coast and the ~20 m isobath.

Nearshore wave climate is a function of all factors that generate and dissipate wave energy (e.g., winds, coastal orientation, continental shelf size, and slope); however, in the Arctic, sea ice plays an additional crucial role in the development and mitigation of wave energy within the coastal margins. Seasonal sea ice forms in early to late fall, with ice first forming in the protected bays and shallows, and eventually merging with basin-wide multi-year and accumulated pack ice and eliminating any surface wave action at the coast, and subsequently breaks up sometime in late spring or early summer. During the transitionary "shoulder seasons" when landfast ice breaks up or forms, wave growth and energy transfer are mitigated by reduced wind-sea surface drag and dissipation by the presence of ice, further complicating the accurate depiction of nearshore wave conditions. Landfast ice is sea ice that is attached to the coastlines or shallow sea floor on the continental shelves and therefore does not drift with currents and wind.

Since the satellite era, it has become increasingly clear that freeze-up and thaw occur later and earlier, respectively, resulting in extended periods over which wave generation can occur (Frey et al., 2015; Thomson and Rogers, 2014; Wang and Overland, 2015). Additionally, minimum sea ice extents, which typically occur in September, are, since the year 2000, decreasing at a rate of 3.4% per decade across the Arctic basin, with the most expansive changes of open water area occurring across the Beaufort Sea and Chukchi Sea coasts (Frey et al., 2015; Stopa et al., 2016; Stroeve and Notz, 2018). The resulting increase in fetch, defined by the time-varying shape and size of the ice pack, has resulted in the emergence of swell energy notwithstanding any changes in wind magnitude, direction, and duration (Stopa et al., 2016; Thomson et al., 2016). Previous works have shown increases in mean and extreme wind speeds, as well as increasing frequency of occurrence of extreme winds in October when landfast sea ice often begins to form. However, due to limited observations, it remains unclear whether such changes exist in overwater winds and if they are driving observed and hindcasted increasing wind-wave energy and swell either offshore or nearshore.

The objectives of this study are twofold. First, to compare trends in median and extreme wave climatology within the nearshore region to those offshore; Second, to illuminate the underlying causes of noted changes. We investigate changes in nearshore wave conditions along a stretch of the Alaska central Beaufort Sea coast where there is renewed interest in nearshore oil exploration and production. The proposed construction of an additional artificial island in the Liberty Prospect area (near the existing Northstar Island) and exploration-supporting infrastructure has raised concerns for potential negative impacts on marine mammals, subsistence whaling, and nearshore habitats, especially around the nearby Boulder Patch. The Boulder Patch

https://doi.org/10.5194/tc-2021-343
Preprint. Discussion started: 29 November 2021

is an ecologically important area within Stefansson Sound believed to support Beaufort Sea's richest and most diverse biological communities (Dunton et al., 1982). A high-resolution SWAN (Simulating WAves Nearshore; Booij et al., 1999) wave model, forced with winds from a state-of-the-art global reanalysis, is calibrated and validated against *in situ* offshore and nearshore wave measurements and used to compute a continuous three-hourly time-series of wave conditions from 1979 through 2019. The model includes newly implemented formulations (Rogers, 2019) to account for limited wave growth and energy dissipation within the Marginal Ice Zone (MIZ).

This manuscript begins with a description of the greater Stefansson Sound region and field measurements obtained therein. The model setup, calibration, and validation are then presented, followed by analyses of changes in hindcasted winds and waves both within the nearshore region of Stefansson Sound and offshore. Limitations and implications are then discussed in the final two sections.

2. Site description

Foggy Island Bay (FIB) is relatively shallow with a mean water depth of ~7 m and is sheltered by several offshore shoals and barrier island complexes (Figure 1). FIB is fronted by the Beaufort Shelf that extends 60 to 120 km offshore with an average depth of 37 m. The slope of the shelf is mild, with bottom slopes typically being ~10^{-3} inshore of the 10 m isobath (Curchister al., 2018). Meteorological conditions along the Beaufort Sea coast are a major controlling factor in determining the physical environment of the entire region. Wind directions are largely bimodal blowing from either east or west, with prevailing winds from the east (Mahoney et al., 2019; Figure 2A). Both regional-scale atmospheric circulation patterns and mesoscale coastal wind phenomena contribute to the distinct wind patterns. Wave directions are similarly bimodal with a predominant direction from the east (Erikson et al., 2020; Figure 2B).

The region experiences subfreezing temperatures for nine months of the year when air temperatures can reach to -45°C (Overland, 2009) and with strong winds can produce even colder wind chills. The mean annual temperature is ~-10°C, but during the summer months, air temperatures occasionally exceed +20°C (Curchitser et al., 2018). Air temperature controls the timing of sea ice formation and breakup.

Sea ice initially forms in the shallows of FIB in late September and early October, then slowly thickens and grows seaward until Beaufort Shelf is ice-covered by the second or third week of October (Figure 3A). In the fall, when the floating ice sheet grows seaward, the ice gradually attaches to the near-freezing seabed, gradually thickens to ~1.7 to 2.2 m by mid-March, and then remains constant through mid-June (Mahoney et al., 2014; Curchister et al., 2018).

Break-up of the nearshore landfast ice zone begins in late May or June and typically disappears by mid-July (Figure 3A). During break-up, coastal rivers discharge warmer fresh sediment-laden water onto the landfast ice hastening its nearshore melting (Dmitrenko et al., 1999). Through June, the offshore sea ice (once attached to land as landfast ice) rapidly breaks up, often sped up by winds, freshening the surface waters while dispersing large amounts of sediment and organic matter into the

https://doi.org/10.5194/tc-2021-343
Preprint. Discussion started: 29 November 2021

The Cryosphere Discussions
Open Access
EGU

water column (Mahoney et al., 2007). Typically, by July, FIB is ice-free, although small floating ice can drift into the waters (Stroeve & Notz, 2018).

Wave conditions are strongly influenced by these seasonal variations of ice concentration and wind speeds (Erikson et al., 2020). During the frozen months from early to mid-November through May, no wave action is observed (Figure 3C). However, once ice concentrations start to decrease, waves begin to emerge in the region (e.g., Thomson et al., 2016). High wave heights increase throughout the open water season due to increase higher wind speeds and larger fetch. The highest wave heights are typically observed in late October when wind speeds are high and ice is not yet present (e.g., Stopa et al., 2012).

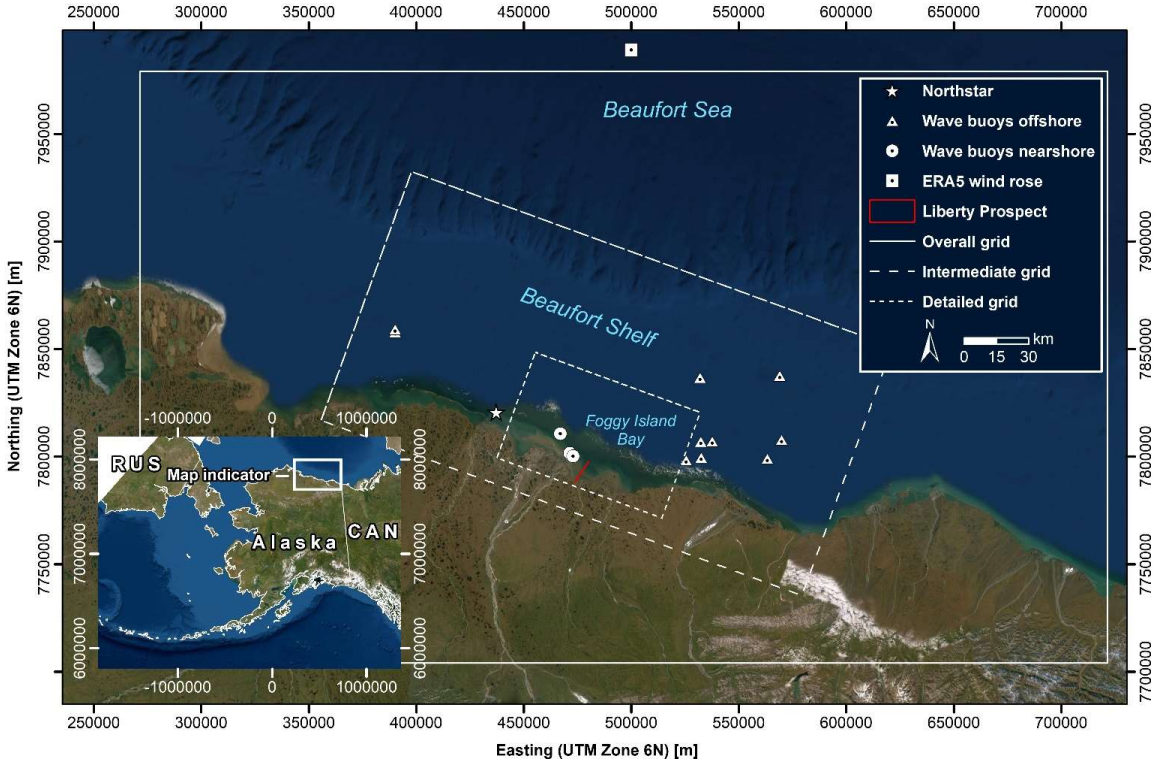

Figure 1. Map showing study area and vicinity including wave buoys used for calibration and validation, Northstar, Liberty Prospect, model grids and the wind rose location. © Esri, DigitalGlobe, GeoEye, Earthstar Geographics,

CNES/Airbus DS, USDA, USGS, AeroGRID, IGN and the GIS User Community

https://doi.org/10.5194/tc-2021-343
Preprint. Discussion started: 29 November 2021

The Cryosphere Discussions
Open Access
EGU

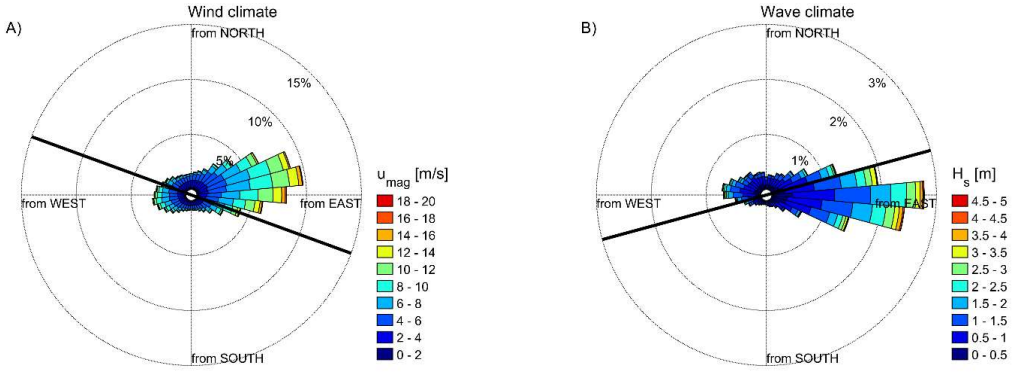

Figure 2. Wind (left; A) and wave (right; B) climate at a single ERA5 output point N72°, W147° for the time period 1979-2019. In panel A the black line depicts the overall coastline orientation of 110°N and in panel B the mean wave direction of 75°N.

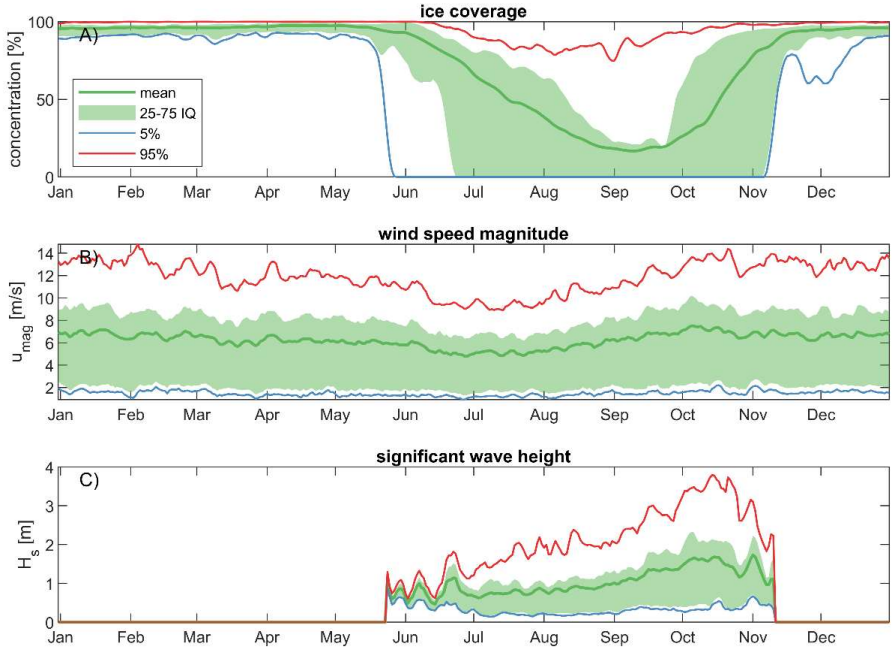

Figure 3. Ice concentrations (A), wind speed magnitude (B) and significant wave height (C) daily-averaged over the time period 1979-2019 for the Stefansson Sound based on ERA5 for the overall domain (see Figure 1 or 4 for the extent of this domain). Each

https://doi.org/10.5194/tc-2021-343
Preprint. Discussion started: 29 November 2021

subplot shows the mean, 5, 25, 75, and 95% exceedance probability. The interquartile range (IQ) is shaded green area between the 25 and 75 percentiles.

3. Materials and Methods

3.1 Data sources

3.1.1. ERA5

ERA5 (Hersbach et al., 2020) is a detailed reanalysis of the global atmosphere, land surface, and ocean waves from 1950 onwards produced by the European Centre for Medium-Range Weather Forecasts (ECMWF). This meteorological dataset provides, among other variables, estimates of atmospheric parameters such as air temperature, pressure, wind, ice concentration, and information on waves over the global oceans at 0.5-degree resolution. The reanalysis combines model data with observations from across the world into a globally complete and consistent dataset using the laws of physics. ERA5 has been shown to perform well in capturing observed weather and climate variability in Alaska and the Arctic (Graham et al., 2019). In this paper, offshore significant wave height (H_s), mean period (T_m), and direction (D_m) are used to drive the SWAN model. Wind conditions (u_{10}, v_{10}) and ice concentration (IC) from this reanalysis dataset are additionally applied across all model domains.

3.1.2. Field measurements

Limited *in situ* observational wave data exist within Beaufort Sea and particularly within Foggy Island Bay. As part of this study, existing wave observations from the 1980s until 2013 were gathered by combing several existing databases. These observations are available via Alaska Ocean Observing System (AOOS; https://aoos.org/). High-quality observations from 2007-2013 were selected to calibrate and validate the model. Data prior to 2007 provided daily wave height estimates measured with a 'yard stick' and therefore deemed insufficiently accurate for this study. With the exception of one shallow-water (~3 m) time-series measurement in 1982 that was located outside the high-resolution model domain (Gallaway, 1983), all previously collected wave observations were in deep water (depth > 20 meters). Therefore, additional measurements were collected as part of the Bureau of Ocean and Energy Management (BOEM) Central Beaufort Sea Wave and Hydrodynamic Modeling Study. Sofar Spotter wave buoys (Raghukumar et al., 2019) were deployed in shallow water for approximately 4 weeks each in the summer of 2019 and 2020. The buoys were set to broadcast standard bulk wave parameters (e.g., H_s, T_p, D_p, etc.) every hour via an Iridium satellite communication network. Three Spotter buoys were used in this study, deployed in 2019 (1x) and 2020 (2x). Spotter #0519 deployed in 2020 was dragged by ice and changed position and is therefore included twice in summary Table 1.

Wave buoy observations collected in 2007-2019 and 2019-2020 are used to calibrate and validate the SWAN grid models (see next section). Measurements collected between 2007 and 2019 during partial ice-cover were split into time-periods for

https://doi.org/10.5194/tc-2021-343
Preprint. Discussion started: 29 November 2021


The Cryosphere Discussions
Open Access
EGU

calibration and validation of the sea ice implementation. In particular, 1,439 time-points during the partial ice season were selected for calibration purposes (~20% of the available timestamps with IC >5%) and 11,430 time stamps in both the open-water and ice season were used for validation. Spotter data collected from within the shallow region of FIB during the 2019 open-water (i.e., ice-free) season were used to calibrate the friction formulations and coefficients. In addition, 2020 nearshore Spotter data were used to validate the finest resolution grid and nearshore wave heights.

Table 1. Overview of wave observations used for calibration and validation purposes in this paper. The name of each observation is a combination of the calendar year of deployment and a letter. Longitude and latitude are coordinates in degrees (WGS84). Depth is in meters relative to mean sea level. The start and end dates (mm-dd) of deployment are indicated. The comment provides more information including which measurement was used for calibration and validation for sea ice coefficients and friction coefficients and formulation.

Name	Longitude	Latitude	Depth [m]	Start	End	Usage
2007_A	-145.13	70.37	36	10-04	12-30	Calibrate Sea ice coef
2007_K	-146.32	70.29	24	10-03	12-30	Sea ice coef
2007_V	-146.14	70.30	27	10-04	12-30	Sea ice coef
2008_A	-146.00	70.37	31	01-01	10-08	Sea ice coef
2008_K	-145.32	70.29	31	01-01	10-08	Sea ice coef
2008_V	-145.13	70.63	55	01-01	10-05	Sea ice coef
2011_A	-146.00	70.37	31	10-02	12-30	Sea ice coef
2011_V	-145.14	70.63	55	10-02	12-30	Sea ice coef
2012_A	-146.00	70.37	31	10-06	12-30	Sea ice coef
2012_B	-149.99	70.80	22	10-03	12-30	Sea ice coef
2012_V	-146.14	70.63	43	10-05	11-30	Sea ice coef
2013_A	-146.00	70.37	31	01-01	10-01	Sea ice coef
2013_B	-149.99	70.81	24	01-01	10-03	Sea ice coef
2019	-147.76	70.32	3	08-06	09-09	Friction coef Spotter by Sofar #0156
2020A	-147.88	70.40	6	07-20	08-12	Friction coef Spotter by Sofar #0518
2020B	-147.76	70.32	3	07-17	08-12	Friction coef Spotter by Sofar #0519-1
2020C	-147.72	70.31	?	07-17	08-12	Friction coef Spotter by Sofar #0519-2

https://doi.org/10.5194/tc-2021-343
Preprint. Discussion started: 29 November 2021

3.2. Model

The spectral wind-wave model SWAN is widely used to compute wavefields over shelf seas, in coastal areas, and in shallow lakes. The accurate estimation of wavefield statistics by such models is essential to various applications in these environments. SWAN computes the evolution of wave action density N = E/σ, where E is the wave variance density spectrum and σ the relative radian frequency, using the action balance equation.

Recently, Rogers (2019) implemented input/output for sea ice in SWAN, a dissipation source term, and scaling of wind input source functions by sea ice. This functionality is built on lessons learned during the implementation of sea ice in WAVEWATCH III (Collins and Rogers, 2017). The formulations use a simple empirical parametric model (polynomial function) for dissipation by sea ice, following Meylan et al. (2014) and Collins and Rogers (2017), which prescribe the dissipation rate as a function dependent on the wave frequency. Thus, the temporal exponential decay rate of energy can be written as:

$$D_{ice} = \frac{S_{ice}}{E} = -2c_g k_i, \quad (1)$$

where S_{ice} is the sea ice sink term, and E is the wave energy spectrum. Here, k_i has units of 1/m and is the linear exponential attenuation rate of wave amplitude in space. Factor 2 provides a conversion from amplitude to energy decay. The group velocity, c_g, enables conversion from spatial decay to temporal decay. S_{ice} and E vary with frequency and direction. In the implementation of Rogers (2019), k_i varies with frequency according to:

$$k_i(f) = c_0 + c_0 f + c_2 f^2 + c_3 f^3 + c_4 f^4 + c_5 f^5 + c_6 f^6, \quad (2)$$

with c_0 to c_6 being the user-defined empirical (calibration) polynomial coefficients.

Furthermore, the scaling of the wind input source functions allows the user to control the scaling of wind input by open water fraction with the variable Ω_{iw} (Rogers, 2019). The default value of Ω_{iw}= 0, used throughout this study, corresponds to the case where wind input is scaled by the total fraction of open water.

These formulations, also referred to as IC4M2, have been implemented in the main sub-version of SWAN since version 41.31, which is the version used in this study. Here, a three-level SWAN nested grid setup is used (Figure 4) with grid resolutions of 5,000, 1,000, and 200 meters for the overall, intermediate and detail grids, respectively.

SWAN is run in third-generation mode and includes parameterizations for wind input, quadruplet interactions, triads, and white-capping. SWAN is run with physics package ST6 (Rogers et al., 2012) that allows for a multiplier on the drag coefficient. Here we base the drag coefficient multiplier on the work of Le Roux (2009), which accounts for differences in air-water temperatures. SWAN normally does not include this effect, but the Le Roux formulation based on temperature difference is included here via the ST6 implementation. Based on the analytical wave height formulation of Le Roux, variations to the wave height because of variations in the drag coefficient multiplier are estimated to be between -10 to +10% (95% confidence interval, CI) or drag coefficient multiplier of ±20%. Wave boundary conditions and meteorological forcing conditions are

https://doi.org/10.5194/tc-2021-343
Preprint. Discussion started: 29 November 2021

The Cryosphere Discussions
Open Access
EGU

based on ERA5. Numerical frequency resolution ranges lognormally from 0.03 Hz up to 2.5 Hz in 46 frequency bins (33.3 – 0.4 seconds). Five-degree bins are used to resolve wave direction.

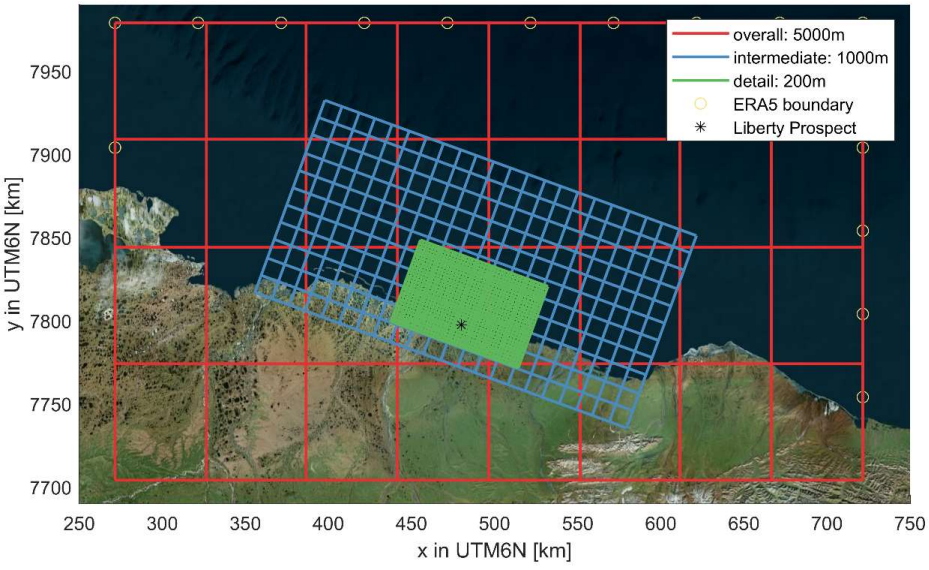

Figure 4. Three-level SWAN model nests with the coarse overall (red), intermediate (blue), and fine detailed grid (green). The model resolution is 10x times denser than as depicted in the figure. ERA5 wave boundary points are presented as circles. Black star denotes the location of the proposed construction of an artificial island in Foggy Island Bay. © Microsoft Bing Maps.

Calibration was performed via the testing of several friction formulations and coefficients. In particular, bottom friction formulations (BFF) of Hasselmann et al. (1973; called JONSWAP), Collins (1972, called Collins-BFF), and Madsen et al. (1988; called Madsen-BFF) were tested. Moreover, several empirical coefficients of the newly implemented ice formulations by Rogers (2019) were tested regarding the empirical (calibration) polynomial coefficients for dissipation and Ω_{iw}.

3.3 Methods

Wave conditions across the Beaufort Sea, Beaufort sound, and FIB were simulated with three-hourly stationary SWAN simulations. First, the model was run over time periods with available field measurements to perform calibration and validation of the friction and empirical ice coefficients. Second, the calibrated SWAN model was used to hindcast wave conditions from 1979 to 2019. Both the open-water (ice concentration, IC<5%) and ice season (IC>5%) were simulated. Years were simulated individually, and once completed, they were combined into one 41-year time-series per grid cell with a temporal resolution of three hours.

https://doi.org/10.5194/tc-2021-343
Preprint. Discussion started: 29 November 2021

205 **3.3.1. Skill scores**

To assess model skill, several metrics were used. In particular, the model bias, mean-absolute-error (MAE; Eq 3), Root-Mean-Square-Error (RMSE; Eq. 4) and scatter index (SCI; Eq. 5) were computed. The latter gives a relative measure of the RMSE compared to the observed variability.

$$MAE = \frac{1}{N}\sum(y_i - x_i) \quad (3)$$

210

$$RMSE = \sqrt{\frac{1}{N}\sum(y_i - x_i)^2} \quad (4)$$

$$SCI = \frac{\sqrt{\frac{1}{N}\sum(y_i - x_i)^2}}{\sqrt{\frac{1}{N}\sum {y_i}^2}}, \quad (5)$$

in which y_i is the computed value, x_i is the observed value, and n is the total number of data points.

3.3.2. Trend analysis

215 Summary statistics of wave height (H_s), wave period (T_m), wave direction (D_m), wave power (P), wave steepness (s), IC, and wind speed (u_{mag}) were computed. The median, 90th% percentile (or 10% exceedance probability), and maximum values for each variable were computed for several daily, monthly, seasonal, and yearly periods. Additionally, the annual count of rough wave days (τ_{ro}), defined as the number of days when H_s exceeds 2.5 m per year (WCRP, 2020) were also computed. Also, the number of open (IC <5% ice) and closed days (IC >85%) were determined for the area of interest.

220 The non-parametric Mann-Kendall (MK; Mann 1945, Kendall 1975) test was then applied to detect monotonic trends, and the magnitude of the trends were calculated with Sen's slope (Sen, 1968). The MK test is a test to statistically assess if there is a monotonic upward or downward trend of the variable of interest over time. The MK test is non-parametric (distribution free) and does not require that the residuals of the fitted regression line be normally distributed. However, the standard *p*-values derived from the MK test assume that the observations are independent realizations. Following the method used by Wang and

225 Swail (2001), the effects of autocorrelations are accounted for in assessing trends and their significance. A pre-whitened time-series (i.e., processed to make it behave statistically like white noise) that possesses the same trend as the original signal is computed and re-computed via an iterative approach to find the best fit line and adjusted *p*-value (Reguero, 2019). The fitted line is Sen's slope.

4. Wave calibration

230 The wave calibration is divided into simulations for observation periods during the open-water season and ice season. This division is made by partitioning the observations based on the mean ice concentration in the area of interest. When the mean ice concentration was higher than 5%, it was deemed part of the ice season. When the mean IC was smaller than 5%, it was

https://doi.org/10.5194/tc-2021-343
Preprint. Discussion started: 29 November 2021

deemed part of the open-water season. In particular, 2019 observations were used for open-water season calibration and ~20% of the available timestamps in the data from 2007-2013 were used for the ice season calibration.

4.1. Open-water season

Observed and computed wave heights and periods for the 2019 measurement period are shown in Figure 5. Individual combinations of bottom friction formulation and friction coefficient are plotted with different colors. Observed wave heights and periods are plotted as black dots. The figure shows strong sensitivity to different friction options used for both the wave height and period. The range of coefficients used for the Madsen et al. (1988) formulation (Madsen-BFF) resulted in too much dissipation due to bottom friction and under-estimated wave heights. Whereas default SWAN values for Collins-BFF and JONSWAP (see Table 2) performed well, the overall best fit, based on visual inspection of the time-series in Fig. 5 and residual plots (not shown) as well as quantitative error statistics, was the formulation of Collins-BFF with a coefficient of 0.020 (RMSE=0.126 m; bias = 0.005m).

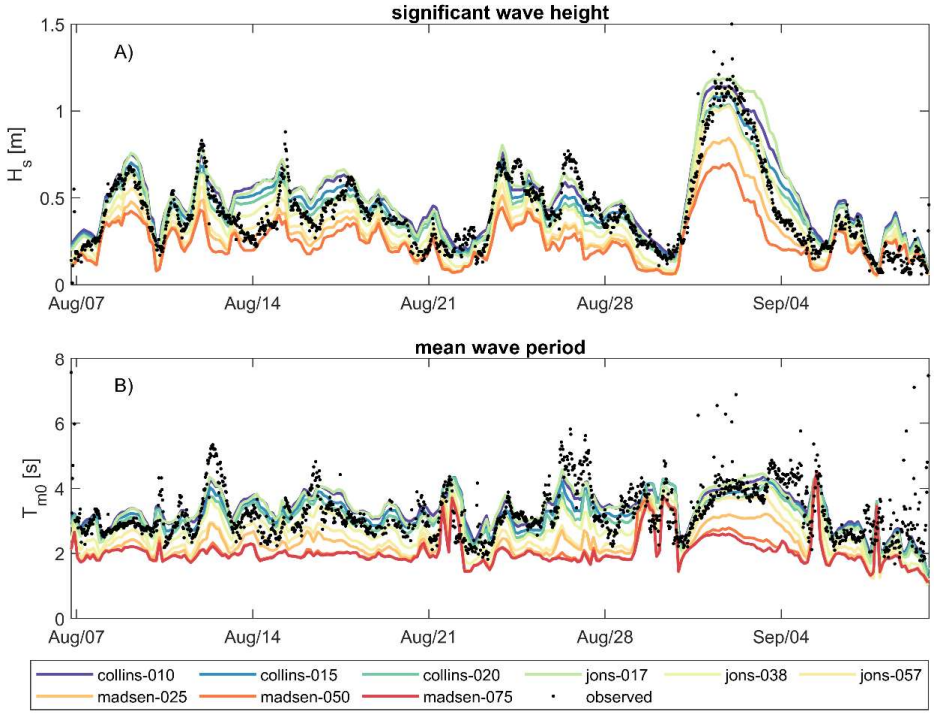

Figure 5. Wave height (panel A) and wave period (panel B) as observed (black dots) and modeled (colored lines) with the detailed domain using various friction formulations and coefficients for the observation period in 2019.

https://doi.org/10.5194/tc-2021-343
Preprint. Discussion started: 29 November 2021

Table 2. Skill scores for computed wave heights using various bottom friction formulations (BFF) and coefficients. The Collins bottom friction formulation (Collins-BFF; Collins, 1972), with a coefficient of 0.020, was chosen for the remainder of this study (denoted in bold). Friction coefficients with a * are SWAN 'default' values. The JONSWAP friction formulations are from Hasselmann et al. (1973), and the Madsen friction formulations are from Madsen et al. (1988).

Friction					
Formulation	**Coefficient**	**RMSE [meter]**	**MAE [meter]**	**Bias [meter]**	**SCI [%]**
Collins-BFF	0.010	0.146	0.297	0.077	11%
Collins-BFF	0.015*	0.129	0.261	0.036	9%
Collins-BFF	**0.020**	**0.126**	**0.256**	**0.005**	**8%**
JONSWAP	0.017 m^2/s^3	0.149	0.302	0.077	11%
JONSWAP	0.038 m^2/s^3*	0.123	0.249	-0.033	8%
JONSWAP	0.057 m^2/s^3	0.151	0.307	-0.092	11%
Madsen-BFF	0.025 m	0.187	0.379	-0.133	14%
Madsen-BFF	0.050 m*	0.227	0.461	-0.169	18%
Madsen-BFF	0.075 m	0.237	0.482	-0.175	18%

4.2. Ice season

Observed and computed wave heights and periods for the 2007 measurement campaign are shown in Figure 6. All individual combinations of empirical ice formulations are plotted with a different color (see Table 2 for a description per combination). Observed wave heights and periods are plotted as black dots. The results show a strong sensitivity to these empirical coefficients. Moreover, the SWAN models miss certain events that ERA5 can reproduce due to the assimilation of altimeter measurements. For example, the event at the end of November 2007, when wave heights around 5-6 meters were observed, was captured in ERA5 but strongly underestimated by SWAN. The observations also have gaps when no waves were observed. Table 2 summarizes model skills for wave height and period for all 13 observations (2007 - 2013) combined. Based on these results, lower IC4M2 coefficient is most appropriate. Values of 1.06E-03 and 2.30E-02, for c_2 and c_4, respectively, in the equation, as Meylan et al. (2014) found for ice floes in the MIZ near Antarctica, resulted in a strong negative bias (i.e., model underestimates; too much dissipation). On the other hand, values of 2.84E-04 and 1.53E-02, as found by Rogers (2019) for pancake and frazil ice, resulted in a better agreement with observations.

https://doi.org/10.5194/tc-2021-343
Preprint. Discussion started: 29 November 2021

The Cryosphere
Discussions
Open Access
EGU

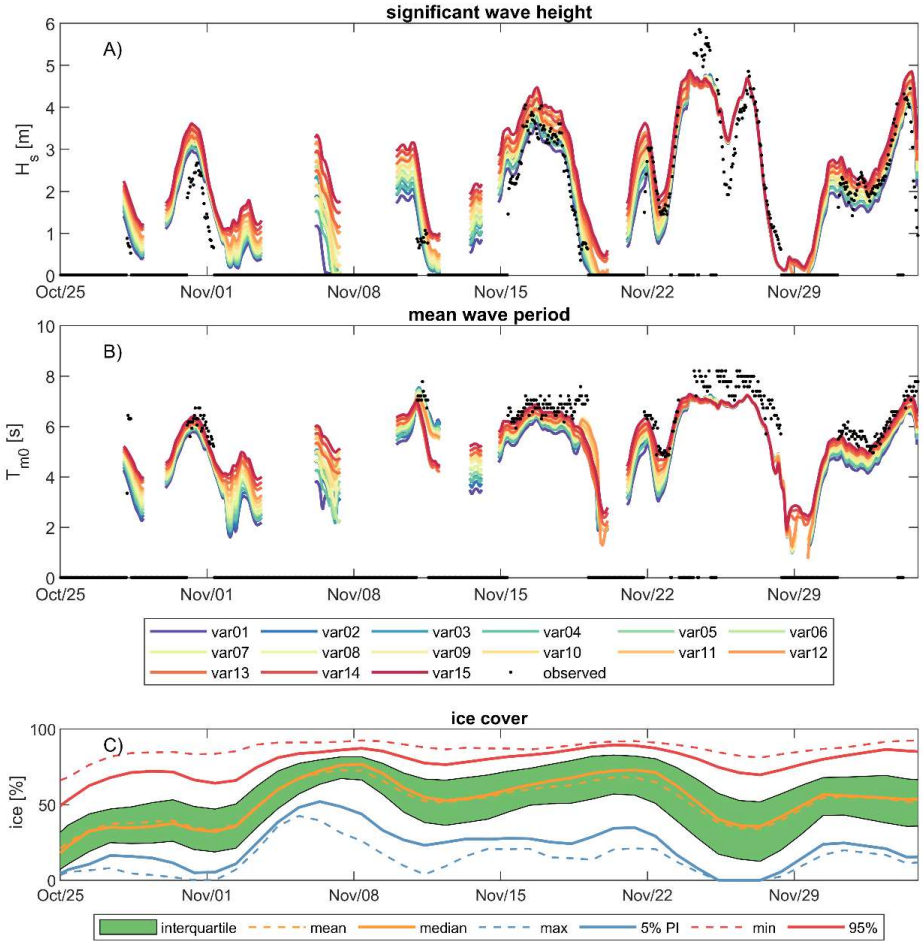

265

Figure 6. Wave height (panel A) and wave period (panel B) as observed (black dots) and modeled (colored lines) with the detailed intermediate domain using various combinations of empirical ice formulations (Table 3) for the observation period in 2019. Ice concentrations (panel C) are high across the domain.

https://doi.org/10.5194/tc-2021-343
Preprint. Discussion started: 29 November 2021


The Cryosphere Discussions
Open Access
EGU

Table 3. Significant wave height model skill for different combinations of empirical ice coefficients describing dissipation and reduction of wave growth. Var07 (bold) is the chosen value for the remainder of this study. All 1,439 observations with at least a mean ice concentration of 5% from 2007-2013 are considered.

Short	IC4M2 (CD2)	IC4M2 (CD4)	Ω_{iw}	RMSE [m]	MAE [m]	SCI [%]	bias [m]
var01	1.06E-03	2.30E-02	0.00	0.707	0.586	26%	-0.586
var02	1.06E-03	2.30E-02	0.50	0.615	0.481	23%	-0.481
var03	1.06E-03	2.30E-02	1.00	0.553	0.394	21%	-0.394
var04	6.72E-04	1.92E-02	0.00	0.627	0.482	23%	-0.482
var05	6.72E-04	1.92E-02	0.50	0.549	0.377	20%	-0.377
var06	6.72E-04	1.92E-02	1.00	0.491	0.285	18%	-0.285
var07	**2.84E-04**	**1.53E-02**	**0.00**	**0.556**	**0.362**	**21%**	**-0.362**
var08	2.84E-04	1.53E-02	0.50	0.492	0.261	18%	-0.250
var09	2.84E-04	1.53E-02	1.00	0.446	0.199	17%	-0.147
var10	0.00E+00	1.15E-02	0.00	0.521	0.284	19%	-0.250
var11	0.00E+00	1.15E-02	0.50	0.471	0.239	18%	-0.122
var12	0.00E+00	1.15E-02	1.00	0.456	0.268	17%	-0.011
var13	0.00E+00	0.00E+00	0.00	0.539	0.338	20%	-0.075
var14	0.00E+00	0.00E+00	0.50	0.538	0.370	20%	0.062
var15	0.00E+00	0.00E+00	1.00	0.549	0.417	20%	0.171

5. Wave validation

5.1 Nearshore validation

Observed and computed wave heights and periods for the 2020 measurement campaign are shown in Figure 7. Similar to previous figures, model results are plotted as color lines and observed data as black dots. The figure shows that generally increasing model resolution improves reproductive skill. In particular, the detail model domain has the lowest RMSE of 0.133 and 0.118 meters for 2020A and 2020B+C, respectively. However, the overall and intermediate model domains also have good model skill for the nearshore Spotter observations. The detailed domain results in a ~20% reduction in RMSE but with an ~80% increase in computation time. Model resolution cannot explain the mismatch for time periods 07/27-08/01 and ~08/06, where larger differences between observations and measurements can be seen.

https://doi.org/10.5194/tc-2021-343
Preprint. Discussion started: 29 November 2021

The Cryosphere Discussions
Open Access
EGU

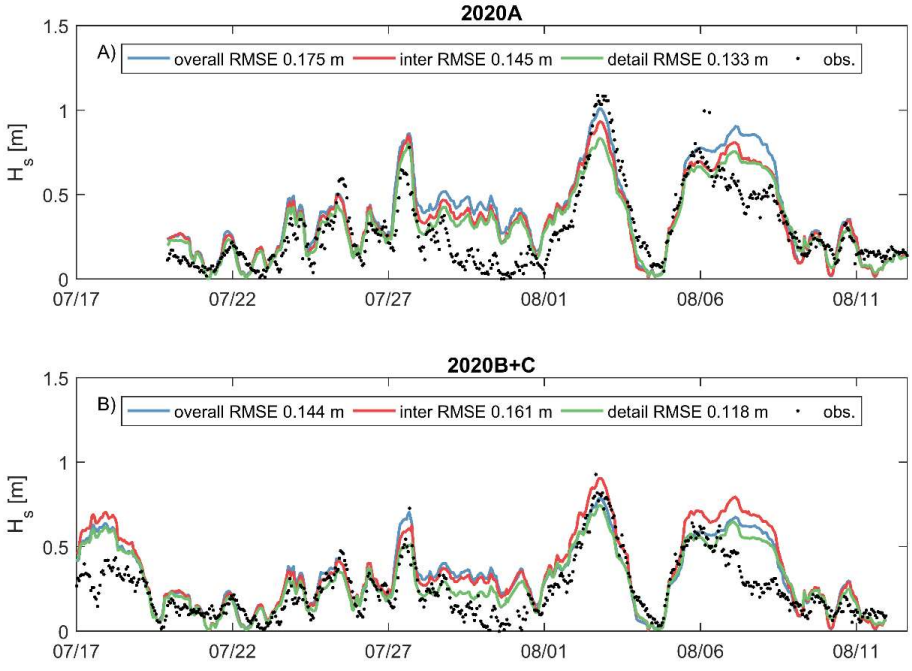

Figure 7. Wave height (panel A) and wave period (panel B) as observed (black dots) and modeled (colored lines) with the detailed intermediate domain using Wave height as observed (black dots) and modeled (colored lines) for the observations in 2020 computed by the overall (red), intermediate (blue) and detailed (green) domain. Upper panel is Spotter #0519-1 and bottom panel is #0519-2. See Figure 1 for the extend and locations of these grids.

5.2. Large-scale validation

The calibration coefficients found in the previous section for the open-water (i.e., friction formulation and coefficient; Collins-BFF of 0.020) and ice season (i.e., empirical coefficients for ice dissipation and reduction on wave growth; var07) are validated for the remaining observations point not used within the calibration period. In particular, 11,430 time stamps in both the open-water and ice season were used for large-scale validation. This approach allows for independent validation of the model. Figure 8 presents scatter density plots for the modeled and observed significant wave height (Figure 8A) and mean wave period (Figure 8B) as modeled with the intermediate grid. The model slightly overestimates both the wave height (bias of 19 cm) and period (1.3 s). SCIs for wave heights and periods are around 30%. This is deemed acceptable to assess changes in the wave climate.

https://doi.org/10.5194/tc-2021-343
Preprint. Discussion started: 29 November 2021

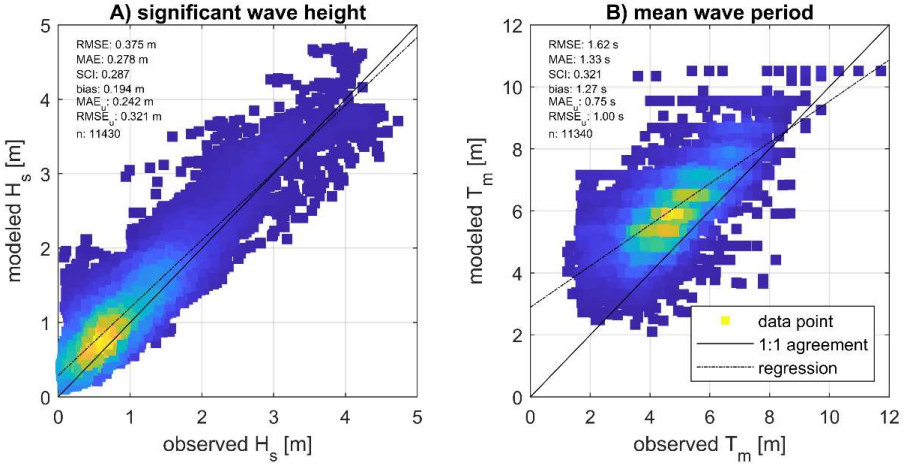

Figure 8. Scatter density plots of the modeled and observed wave parameters for >10,000 timestamps for the combined dataset of observations collected between 2007-2013 for the intermediate domain. A) Significant wave height and B) mean wave period.

6. Changes in wave and meteorological climatologies

In this section, a 41 year hindcast of waves simulated with SWAN are analyzed. First, changes in meteorological conditions, including changes in ice concentration and the number of open-water days and historical winds, are presented (Figures 9 and 10). Second, changes in wave height, period, wave power and direction, are visualized and quantified. Table 4 presents an overview of the results per month, season, and year. Figure 11 presents an overview of the main changes in climate for September, October, and November (SON).

6.1. Changes in meteorological climate

6.1.1. Wind

Wind speeds and direction vary from month to month, with higher extremes between ~October and May. Figure 9 presents the number of days during which the study area had a Beaufort scale of <4 (gentle breeze), 4 (moderate breeze), 5 (fresh breeze), 6 (strong breeze), and >6 (gale force) based on the wind speed magnitude in ERA5. Although there is year-to-year variability, visually, no trends emerge. Spatial variability (not shown) reveals that median wind speeds are fairly constant along the coast but decrease in the cross-shore direction from sea to land. In contrast, annual extreme wind speeds are higher in the southeast corner of the domain with an annual wind speed of close to 21 m/s. The MK test of the annual extreme winds reveals a statistically *insignificant* median trend of +0.01 m/s per year (or less than +0.1% per year).

https://doi.org/10.5194/tc-2021-343
Preprint. Discussion started: 29 November 2021

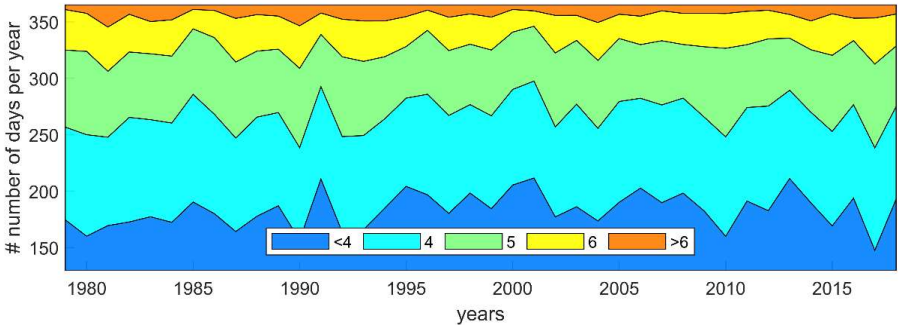

Figure 9. The number of days with Beaufort scale <4 (gentle breeze), 4 (moderate breeze), 5 (fresh breeze), 6 (strong breeze) and >6 (gale force) as simulated by ERA5 for the area of interest. Data are based on the average wind speed for the intermediate domain.

6.1.1. Sea ice

Ice concentration varies considerably from month to month. As shown in Figure 3A, the maximum duration of the open water season is from Jun-Nov with the lowest concentration around Sep-Oct. Figure 10 presents the number of days per year during which the area of interest (intermediate domain, see Figure 1 for extend, part of Beaufort Shelf) was fully closed (IC>85%), open (IC<5%), or was in an intermediate state. The trend lines reveal a large decrease in the number of days the FIB area was covered with ice and a similar increase in the number of days it was fully ice-free. For example, in 1979, on average, the area was closed for ~250 days and only fully open for a few weeks. In 2019, 41 years later, this has changed to 195 and 110 days, respectively. This equates to an eightfold increase in the number of open water days. This increase in open water days is driven both by earlier sea ice break-up and later freeze-up.

Moreover, the MK test reveals a statistically significant trend of decreasing median IC of -1.3 and -1.7% per year for the summer (June, July, August; JJA) and fall (September, October, November; SON), respectively. Figure 11A presents the 41-year median IC for SON and the trend of IC for SON (Figure 11B) for the area of interest. Spatial variability reveals that median ice concentrations (IC_{50}) to be the lowest (close to zero) in the northwest of the area of interest and highest in the southeast (around 25%). Larger negative gradient occurs closer to the shoreline (around the 10-meter depth contour) and in the areas with generally higher concentrations. IC_{50} trends have a statistically significant trend across the area of interest. Table 3 shows similar patterns as seen visually. Statistically significant decreasing trends in ice concentration occur in months July-November, with October being the month with the most significant negative trend.

https://doi.org/10.5194/tc-2021-343
Preprint. Discussion started: 29 November 2021

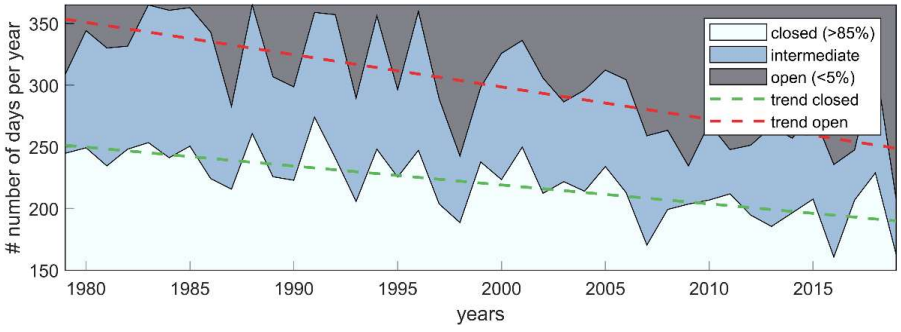

Figure 10. The number of closed (IC>85%), intermediate, and open (IC<5%) days based on the percentage ice cover as simulated by ERA5 for the area of interest (intermediate domain, see Figure 1 for extend, part of Beaufort Shelf). Trend lines for the number of closed days (green) and open days (red) are presented as dashed lines. Data are based on a spatial average of the intermediate domain.

6.2. Changes in wave climate

6.2.1. Wave heights

Wave heights vary widely from month to month because of the seasonality of the IC. As shown in Figure 3, waves occur mostly from late-May to November, depending on the ice concentration. Figure 12A presents the daily median wave height ($H_{s,50}$) for 41 years based on simulated conditions averaged across FIB. In general, no waves are present during the months of December to June, when ice concentration is near 100%. Strong year-to-year variations are evident, but visually it is clear that wave heights have increased substantially in the last forty years. In 1979, H_{s50} higher than 0.5 meters were present only from ~Aug-Oct. In 2019, this period extended to ~Jul-Nov. This pattern correlates strongly with changes in IC in the area (correlation coefficient r of -0.70 for daily H_{s50} and IC_{50}).

These visually observed trends are quantified by the MK test of the 10% exceedance wave height (H_{s90}). Spatial variability of $H_{s,90,}$ and trends for the fall season (SON) are presented in Figure 11CD. Wave heights are higher in the northwest (Figure 11C). This is a similar pattern as seen in the IC shown in Figure 11A. Moreover, a clear trend of increasing $H_{s,90}$ can be seen in Figure 11D. There is hardly any alongshore variability of the increasing trend, however, there is a cross-shore variability with larger increases of H_{s90} offshore than closer the shoreline. The increase in the $H_{s,90}$ is estimated to be around +2.0 ± 0.3%[1] per year (or 3.92 ± 1.06 cm/year). Table 3 presents the median in Sen's trend values for the $H_{s,90}$ for all months, seasons, and annually. These larger ($H_{s,90}$) waves mainly occur in September and October, with a median value of around 2.0 and 2.4 m respectively for Sep and Oct based on the 41-year long hindcast. For October, $H_{s,90}$ is increasing by 6.5 ± 1.7 cm per year (or

[1] Throughout this paper, median trend values are reported, including 1x standard deviation depicted with ±.

https://doi.org/10.5194/tc-2021-343
Preprint. Discussion started: 29 November 2021

+2.7 ± 0.7 % per year). This pattern correlates with the largest decrease in the IC. In particular, a negative correlation of 0.87 ± 0.02 is found for the entire dataset for monthly $H_{s,90,}$ and IC_{50}.

Similar trends are found for the more extreme wave conditions. In particular, the annual maximum wave height ($H_{s,max}$) and the number of rough days (τ_{ro}), were computed for the dataset of 41 years of simulated conditions in FIB. Figure 13A presents the $H_{s,max}$ across FIB as a function of time. The spatial median annual $H_{s,max}$ is depicted as black dots and the spatial variability of the annual $H_{s,max}$ is depicted as uncertainty bars. Strong year-to-year variability is visible; however, a statistically significant increasing trend of around 4.1 cm per year (or +1.1% per year) was found, resulting in an increase of a spatially-median $H_{s,max}$ from 2.90 meters in 1979 to 4.62 meter in 2019. Similar to the $H_{s,90}$ during SON (Figure 11C), annual $H_{s,max}$ have a cross-shore instead of alongshore variation. Closer to the shoreline, processes such as dissipation, white-capping, and breaking dissipate wave energy. This depth-induced saturation aligns very closely with the 10-meter depth contour. Within the shallow FIB, wave height tends to have a maximum of ~1.9 meters, implying a depth-induced saturation that corresponds to height/water depth ratio (γ) of 0.4 (depth is ~5 meters). The rather low γ value (typically γ ~0.6-0.78, Battjes and Janssen, 1978) suggests that bottom friction and white-capping by strong winds play an important role in wave energy dissipation near the shore.

Moreover, storms seem to be happening later and later in the calendar year. An analysis identifying per calendar year, the annual maximum wave height of that year and associated storm date, resulted that in 1979, the average storm date occurred on September 24 (day 269), in 2019 this has increased to October 15 (day 289). This shifts the average storm date 20 days later in the calendar year and results in storms with generally higher wind speeds on top of the general decreasing IC (Figure 13B). Increasing occurrences of high wave events, $\tau_{ro,}$ are also identified. Within the simulated 41 years, a statistically significant trend of 0.24 ± 0.10 days per year (or +4.0 ± 1.7 % per year) was determined. This equates to an increase from 1.5 to 13.1 days each year with high wave events in the offshore region. These rough days mainly occur during the fall months of September and October (see also Table 3).

6.2.2. Wave periods and steepness

Figure 11EF presents the median wave period and computed Sen's trend for the fall months. The median wave period varies slightly from offshore to nearshore, with offshore values reaching as high as 4.7 seconds and nearshore values as low as 3.1 seconds. The wave period tends to increase over the analyzed period, and the trend is statistically significant. The increase of T_m varies spatially, with little increase in the shallow areas of FIB up to an increase of 0.03 seconds per year in the deeper offshore parts of the Beaufort Sea. This increase in period is relatively small compared to the median value (i.e., increase of +0.51 ± 0.13 % per year). On the other hand, the median wave steepness of 0.0536 varies slightly in the cross-shore direction (not shown). The Sen's trends of the wave steepness are all statistically insignificant and minor (-0.15 to +0.23 % per year for 97.5% and 2.5% exceedance). Therefore, based on the model results, the wave period increases proportionally with the wave height while maintaining similar wave steepness.

https://doi.org/10.5194/tc-2021-343
Preprint. Discussion started: 29 November 2021

6.2.3. Wave direction

Figure 11 GH presents the annual median wave direction and computed Sen's trend. Offshore waves have a mean incident wave direction of 70-75° (nautical convention, clockwise from geographic north; i.e., traveling from northeast towards the southwest) near the 100-meter isobath. This is (unsurprisingly) identical to the ERA5 wave rose of Figure 2. Hence, incident wave directions in the offshore region strongly reflect the boundary conditions. In shallower waters approaching the shore, the waves refract towards the coastline resulting in a mean wave direction of 48-54° (25-75% percentile) around the 10-meter isobath. Computed Sen's trends show counterclockwise rotation up to 0.39°/year. These trends are larger closer to the shore in shallower water, and statistically significant. Closer to the offshore boundary, the trends are closer to 0°/year but are statistically insignificant. Table 3 presents the breakdown of the median wave direction over all the different months and time periods. The median wave direction hardly changes for any of the analyzed months. However, for the seasons and yearly median wave direction, a negative trend is statistically significant.

6.2.4. Wave power

Figure 14 presents the cumulative yearly wave power per month averaged over all the years simulated. Wave power is highest offshore in deep water and reduces closer to the shoreline. At the 10-meter depth contour, the average cumulative yearly wave power is ~ 70% of the offshore wave power. At the 2-meter depth contour, this decreases to ~ 25%. Figure 15 presents the cumulative wave power at Liberty Prospect in FIB. Five-year smoothed values for cumulative power and mean ice concentration in the shallow FIB have a strong negative correlation of -0.986. The yearly cumulative wave power has increased five-fold over the 41 years analyzed. Also, the computed trend reveals a statistically significant increase in the wave power which is in absolute terms the largest offshore and less in the shallow parts of FIB. However, in relative terms, the increase in wave power is almost constant across the domain. In particular, a statistically significant Sen's trend of 3.9 ± 0.2 % per year is computed for the offshore compared to 3.8 ± 0.2 % per year at the 10-meter depth contour. Table 3 presents the breakdown of the mean wave power over all the different months and time periods. Average wave power is small and hardly changes for the months Dec-June. For months July-Nov there is a statistically significant increasing trend in the wave power reaching a maximum in October. Similar trends emerge with dominant months July, August, September, October, and November, explaining 93% of the wave power together, and this importance hardly varies in the cross-shore direction or with time.

https://doi.org/10.5194/tc-2021-343
Preprint. Discussion started: 29 November 2021

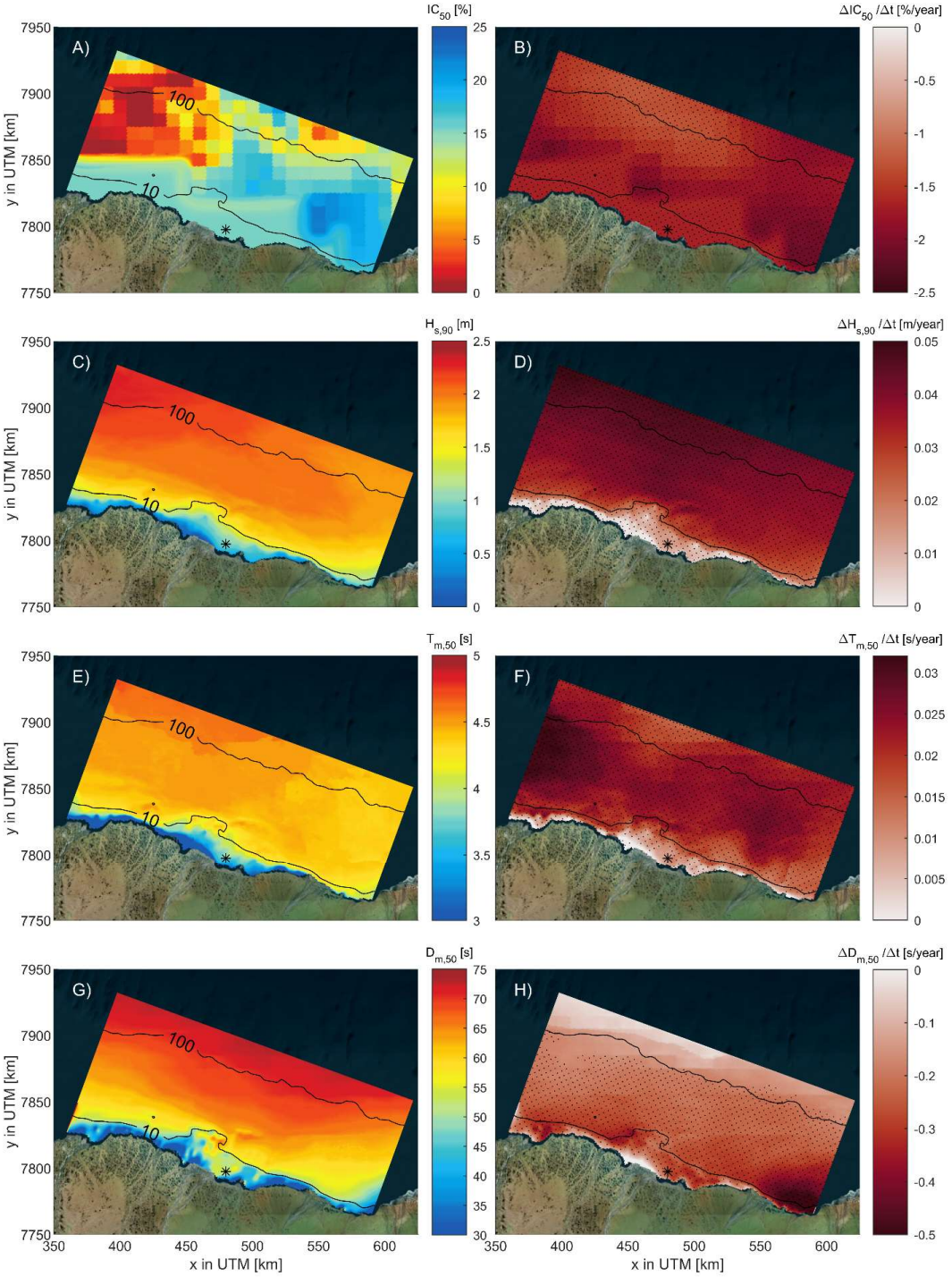

https://doi.org/10.5194/tc-2021-343
Preprint. Discussion started: 29 November 2021

The Cryosphere Discussions
Open Access
EGU

Figure 11. Overview plot of the median value over 41 years of intermediate simulation for ice concentration (IC50; panel A), 10% exceedance probability wave height (Hs90; panel C), median wave period (Tm50; panel E) and median wave direction (Dm50; panel G). Sen's trend (panels B, D, F, H) for the same parameters in the Fall season (SON). Statistically significant trends are stippled. Contour lines are the 100-meter and 10-meter water depths. The white star is the proposed location of an artificial island construction in FIB. © Microsoft Bing Maps.

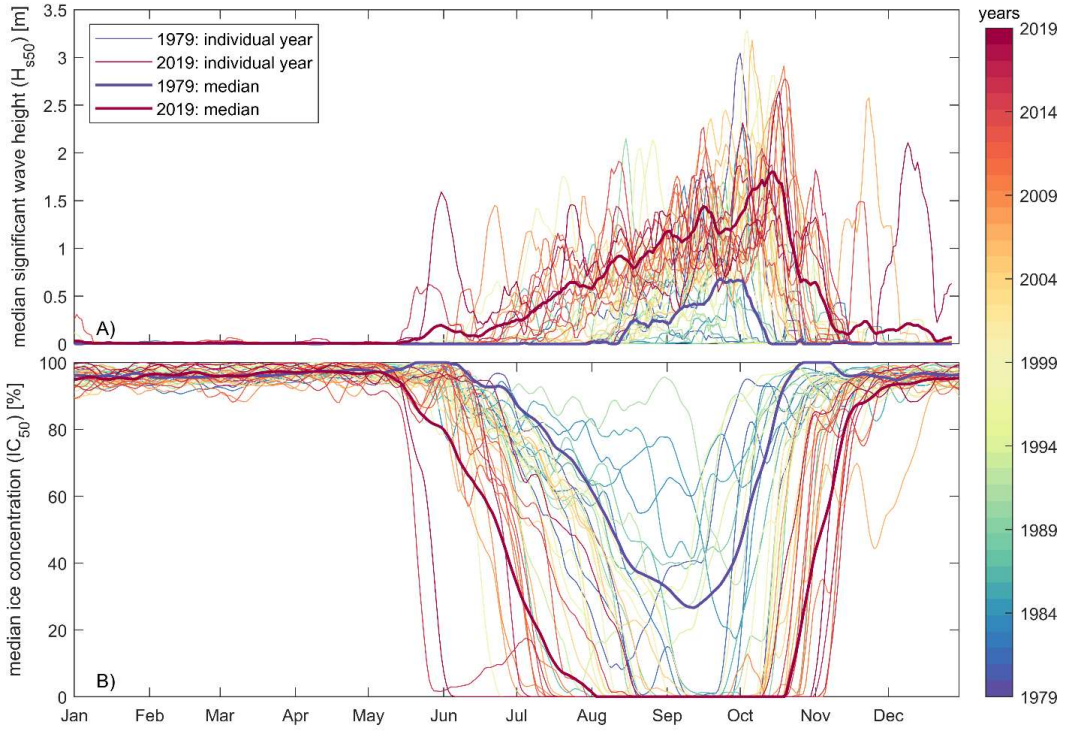

Figure 12. Time-series of the daily median wave height (Hs_{50}) for 41 years of wave data across Foggy Island Bay as simulated by the intermediate SWAN domain (panel A) and daily median ice concentration (panel B). Time series are smoothed by applying a moving weekly filter. The median estimate for 1979 and 2019 is based on a linear fit per day of the individual years.

https://doi.org/10.5194/tc-2021-343
Preprint. Discussion started: 29 November 2021

The Cryosphere Discussions
Open Access
EGU

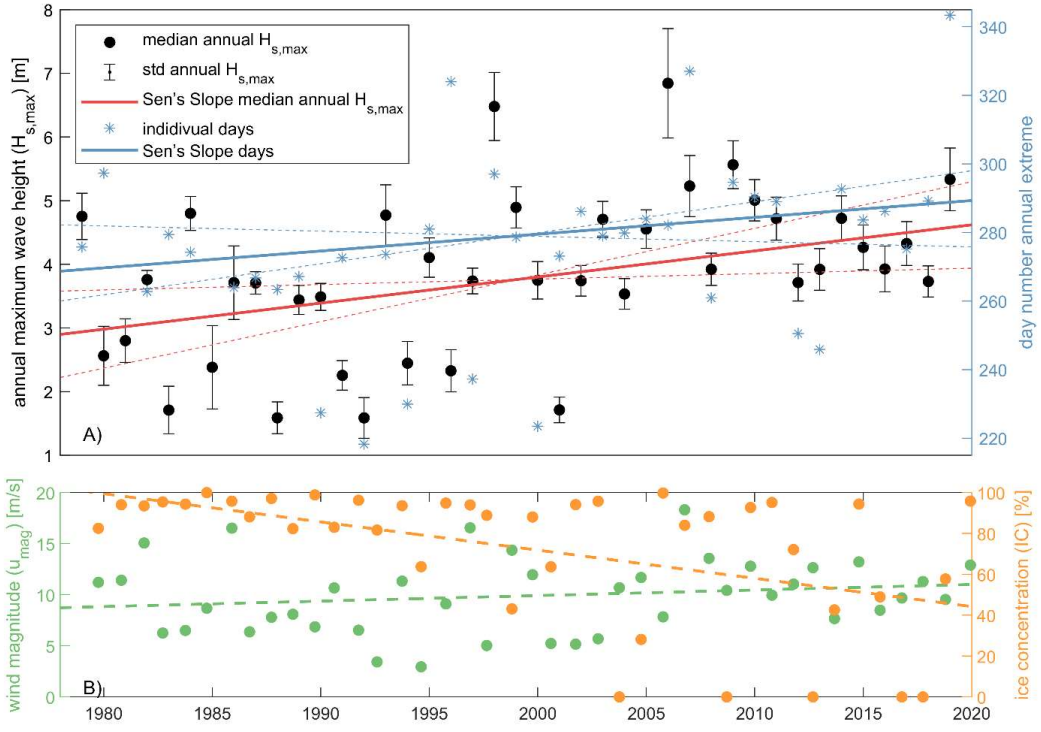

Figure 13. Panel A. Time-series of the annual maximum wave height ($H_{s,max}$) over the last forty years as simulated with SWAN for the intermediate domain with an estimate of day number of the associated peak. The range represents one standard deviation (std) based on spatial variability within the domain. The solid line is the Sen slope including the dashed uncertainty range for an alpha of 0.05 (dashed lines). Panel B. ice concentration and wind speed during the storm based on ERA5 (circles) including linear fit (dashed lines).

https://doi.org/10.5194/tc-2021-343
Preprint. Discussion started: 29 November 2021

The Cryosphere
Discussions
Open Access
EGU

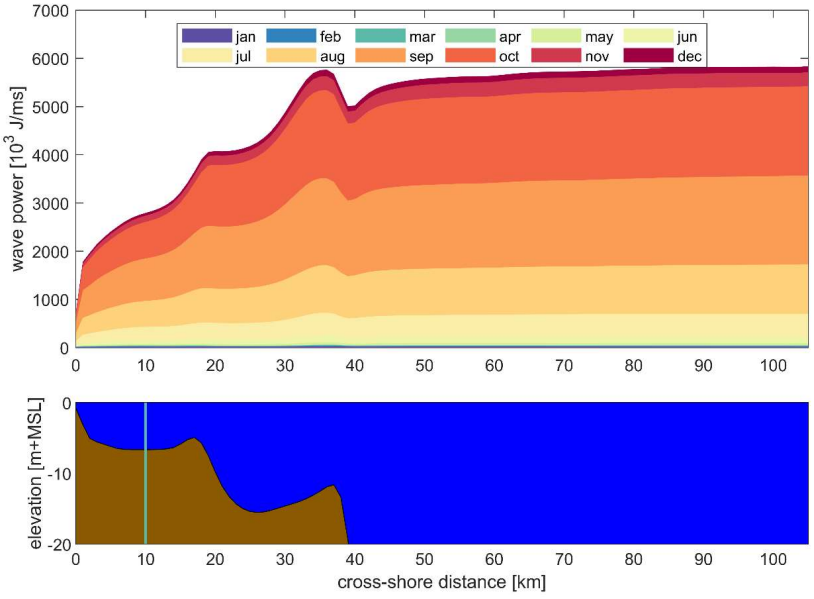

435 **Figure 14. Median over 41 years of monthly cumulative wave power (P) along a transects from nearshore (left) to offshore (right). Different colors represent different months and are cumulative (panel A). Associated bathymetry and water depth (panel B).**

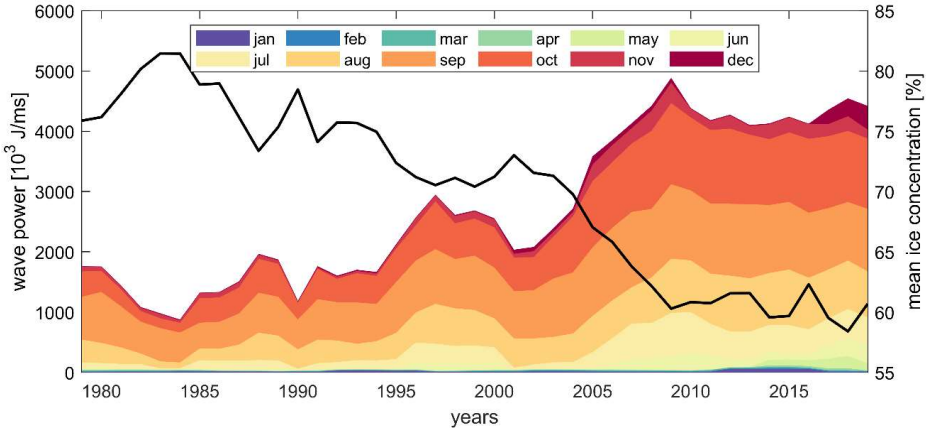

Figure 15. Yearly cumulative wave power (P) smoothed over five-year moving windows at the Liberty Prospect in Foggy Island Bay. Different colors represent different months. Black line is the yearly mean five-year smoothed ice concentration.

440

https://doi.org/10.5194/tc-2021-343
Preprint. Discussion started: 29 November 2021

The Cryosphere Discussions
Open Access
EGU

Table 4. Trend analysis of the median ice concentration (IC_{50}), 90th percentile wave height ($H_{s,90}$), median wave period ($T_{m,50}$), mean wave power (P), median wave direction ($D_{m,50}$) and the number of rough days (τ_{r0}) based on values of the intermediate domain. Median and mean values computed over the entire forty years of simulated data. Computed Sen's trends where the majority of grid cells show a statistically significant trend (assuming alpha of 0.05) are depicted in bold otherwise the trend is shown in normal black color.

	ice_{50}		$H_{s,90}$		$T_{m,50}$		P		$D_{m,50}$		τ_{r0}	
period	Median. [%]	Trend [%/year]	Median [m]	Trend [cm/year]	Median [s]	Trend [s/year]	Mean [J/ms]	Trend [J/ms/year]	Median [deg]	Trend [deg /year]	Median [days]	Trend [days/year]
jan	95.8 ± 0.3	**-0.06 ± 0.01**	0.02 ± 0.00	0.0 ± 0.0	5.7 ± 0.8	0.04 ± 0.67	15 ± 3	0.1 ± 0.0	59.7 ± 8.6	-0.16 ± 0.24	0.00 ± 0.00	0.00 ± 0.00
feb	96.1 ± 0.3	-0.01 ± 0.01	0.02 ± 0.00	0.0 ± 0.0	5.1 ± 0.5	0.08 ± 0.06	12 ± 2	0.1 ± 0.0	62.0 ± 8.7	-0.08 ± 0.26	0.00 ± 0.00	0.00 ± 0.00
march	96.3 ± 0.3	-0.01 ± 0.01	0.02 ± 0.00	0.0 ± 0.0	4.2 ± 0.4	-0.31 ± 0.16	9 ± 1	0.0 ± 0.0	56.1 ± 7.2	-0.31 ± 0.20	0.00 ± 0.00	0.00 ± 0.00
april	97.3 ± 0.2	-0.00 ± 0.01	0.01 ± 0.00	0.0 ± 0.0	5.1 ± 0.2	0.12 ± 0.15	8 ± 1	0.1 ± 0.0	65.3 ± 5.6	-0.07 ± 0.11	0.00 ± 0.00	0.00 ± 0.00
may	96.9 ± 0.3	**-0.07 ± 0.03**	0.01 ± 0.00	-0.0 ± 0.0	5.4 ± 0.7	-0.03 ± 0.13	7 ± 1	-0.0 ± 0.0	67.3 ± 5.4	-0.07 ± 0.14	0.00 ± 0.00	0.00 ± 0.00
june	85.0 ± 1.5	**-0.33 ± 0.08**	0.02 ± 0.00	**0.1 ± 0.0**	5.7 ± 0.7	-0.01 ± 0.03	9 ± 2	**0.7 ± 0.4**	72.2 ± 7.4	-0.03 ± 0.24	0.00 ± 0.00	0.00 ± 0.00
july	49.3 ± 9.4	**-1.22 ± 0.09**	0.20 ± 0.16	**2.0 ± 0.7**	3.8 ± 0.4	0.00 ± 0.02	254 ± 136	**18.0 ± 7.6**	60.5 ± 17.7	-0.21 ± 0.44	0.00 ± 0.00	0.00 ± 0.00
aug	0.2 ± 2.3	**-0.33 ± 0.19**	1.30 ± 0.24	**2.9 ± 0.6**	3.9 ± 0.3	**0.02 ± 0.01**	1001 ± 230	**50.2 ± 10.3**	32.6 ± 9.7	-0.12 ± 0.64	0.00 ± 0.02	**0.00 ± 0.00**
sept	0.0 ± 0.0	**0.00 ± 0.00**	2.00 ± 0.40	**2.3 ± 0.8**	4.3 ± 0.4	**0.02 ± 0.01**	2372 ± 539	**53.1 ± 13.1**	47.5 ± 9.6	-0.14 ± 0.15	1.50 ± 0.69	**0.04 ± 0.02**
oct	13.8 ± 7.0	**-1.59 ± 0.25**	2.43 ± 0.54	**6.5 ± 1.7**	4.6 ± 0.4	**0.02 ± 0.01**	2286 ± 591	**93.7 ± 23.2**	55.8 ± 11.4	-0.26 ± 0.18	3.00 ± 1.29	**0.12 ± 0.05**
nov	92.2 ± 0.7	**-0.34 ± 0.04**	0.04 ± 0.00	**0.1 ± 0.0**	4.5 ± 0.4	-0.01 ± 0.02	77 ± 23	**4.3 ± 1.2**	60.7 ± 6.6	-0.35 ± 0.26	0.00 ± 0.00	**0.00 ± 0.00**
dec	95.6 ± 0.4	-0.04 ± 0.02	0.02 ± 0.00	0.0 ± 0.0	5.2 ± 0.8	-0.07 ± 0.06	14 ± 2	0.0 ± 0.0	58.2 ± 9.1	-0.39 ± 0.24	0.00 ± 0.00	0.00 ± 0.00
DJF	95.8 ± 0.3	**-0.04 ± 0.01**	0.02 ± 0.00	0.0 ± 0.0	5.2 ± 0.7	-0.01 ± 0.04	14 ± 2	0.1 ± 0.0	60.9 ± 11.8	0.07 ± 0.30	0.00 ± 0.00	0.00 ± 0.00
MAM	96.8 ± 0.2	-0.02 ± 0.01	0.02 ± 0.00	0.0 ± 0.0	5.6 ± 0.7	-0.04 ± 0.11	9 ± 1	0.1 ± 0.0	66.4 ± 6.3	0.05 ± 0.10	0.00 ± 0.00	0.00 ± 0.00
JJA	50.0 ± 9.3	**-1.27 ± 0.08**	0.74 ± 0.20	**3.0 ± 0.6**	3.9 ± 0.3	0.01 ± 0.01	453 ± 133	29.6 ± 6.3	65.4 ± 10.5	-0.28 ± 0.15	0.00 ± 0.04	**0.00 ± 0.00**
SON	14.6 ± 5.7	**-1.67 ± 0.22**	1.95 ± 0.41	**3.9 ± 1.1**	4.4 ± 0.4	**0.02 ± 0.01**	1682 ± 403	**54.4 ± 13.4**	57.4 ± 11.7	-0.27 ± 0.11	4.75 ± 2.12	**0.18 ± 0.08**
yearly	92.9 ± 0.4	**-0.14 ± 0.02**	1.00 ± 0.19	**3.2 ± 0.6**	4.3 ± 0.4	**0.01 ± 0.01**	589 ± 138	**24.3 ± 5.4**	65.7 ± 10.2	**-0.22 ± 0.09**	6.00 ± 2.49	**0.24 ± 0.10**

https://doi.org/10.5194/tc-2021-343
Preprint. Discussion started: 29 November 2021

7. Discussion

The validation presented here shows that the constructed SWAN model can reproduce waves during the open water and MIZ seasons. This reproductive skill has been achieved by forcing the model with ERA5 meteorology and with the inclusion of air/sea temperature differences (Le Roux, 2009) and new formulations by Rogers (2019) that account for the effect of ice on (reduced) wave growth and dissipation. An efficient and accurate model-based approach allowed for the continuous 41-year simulations of waves across Alaska's central Beaufort Sea coast and the detailed quantification of changes in the wave climate across the seasons in shallower water than previous studies analyzed.

In current literature, there is a consensus that larger ice-free areas, which are persisting longer into the autumn, force higher sea states across the Beaufort Sea (e.g., Thomson et al., 2016; Liu et al., 2016; Stopa et al., 2016). To our knowledge, no previous study has rigorously quantified how wave patterns vary within the near-and inshore regions of the central Alaska Beaufort Sea and across different seasons over the 41-year simulation period. Within the Beaufort-Chukchi Seas, Thomson et al. (2016) found that altimeter-derived measurements of wave energy increased between 2007 and 2014 and that modeled wave heights increased by 1 cm/year. Stopa et al. (2016) estimated an increase in wave heights up to 1% per year between 1992 and 2014. Findings of listed authors contrasts with this study which suggests larger increases in wave heights over time. In particular, H_{s50} increased by 6%, and H_{s90} and $H_{s,max}$ increased up to 3 and 1%, respectively, over the 41-year hindcast period. We hypothesize that trends are strongly influenced by specifics of the analysis method, different wind and ice boundary conditions, locations and spatial extents, and the time frame considered, and therefore different studies should be compared qualitatively instead of quantitatively.

Nearshore wave hindcasting is sensitive to wind forcing, dissipative/restrictive effects by ice, and boundary conditions from larger-scale models. Similar to several previous studies (e.g., Overeem et al., 2011; Barnhart et al., 2014; Stopa et al., 2016; Erikson et al., 2020), this study found that sea ice minimum now occurs later in Fall, when the wind speeds also increase, which creates more favorable conditions for wave development. However, wind speed magnitudes and thus wave heights might be underestimated due to known biases in extreme wind speeds. For example, Liu et al., 2016 found underestimations of ERA-interim for the Arctic Ocean. Moreover, validation of ERA5 wind speeds at Prudhoe Bay shows an underestimation during storm conditions (see supplementary material). In contrast, wave energy may be over-estimated during break-up and freeze-up due to poorly resolved ice concentrations within the nearshore (e.g., ERA5 ice concentrations used in this study are on a scale of ~50km, compared to the intermediate model domain of ~250 km by ~100 km). However, because the number of days over which break-up and freeze-up occurs is small and getting smaller relative to the overall length of the expanding open-water season. Therefore, it is expected that the lack of resolution in ice concentration to have a minor impact on the assessment of annual cumulative wave energy. IC less than 100% for Jan-May are arguably due to ERA5 reanalysis uncertainties since these conflict with *in situ* observations.

https://doi.org/10.5194/tc-2021-343
Preprint. Discussion started: 29 November 2021

The depth-induced saturation limit of wave heights around 10 meters in the shallow waters of FIB appears to be a result of the combination of depth-induced surf breaking, bottom friction, and white-capping during the open water season, sea ice concentrations during break-up and re-freeze, and is dependent on specific numerical settings in the model. In this study, default values in SWAN for white-capping via ST6 physics and depth-induced breaking in combination with calibrated bottom friction and empirical ice coefficients were used. Further validation and calibration of *in situ* measurements of wave extremes (in the presence of floating ice) will provide invaluable insights into wave physics. More information on nearshore waves, combined with more reliable data on open-water conditions for wind and ice, is vital in understanding these complicated air-sea interactions and feedback processes. For example, Thomson et al. (2016) suggested that waves may be an important mechanism in the re-freezing of ice in the autumn.

Results suggest that wave heights and wave power increased significantly over the past 41 years; however, only minor trends in median wave period and wave steepness were found. Thomson & Rogers (2014) discussed the emergence of swell in the Beaufort–Chukchi Sea domain. Thomson et al. (2016) showed with a local wind hindcast that for recent years (2004, 2006, 2012, and 2014) the wave periods are still short relative to other oceans, which indicates that the sea state of any given ice-free location in the domain is still dominated by local wind waves. Also, a wave model hindcast by the same authors showed a statistically significant trend of 0.04 seconds for the peak wave period over the years 1992-2014. This trend is comparable to the trend found in these results of T_{m50} of 0.03 seconds over the period 1979-2019 for the fall. Moreover, the in this study computed counterclockwise change in wave direction was also reported by others (e.g., Erikson et al., 2016, 2020)

Climate change-induced trends of increasing temperatures and decreasing ice concentrations and extents are expected to continue based on the latest global climate models (e.g., Notz, 2020; Zanowski et al., 2021). It is thus expected the decreasing ice concentrations will result in a further increase of wave heights, periods, and yearly cumulative wave power for Alaska's central Beaufort Sea coast. It is unclear how extremes will change since storms are driven by the combined effect of ice and wind. Continued changes in the wave climate will also likely accelerate historical trends in changes to barrier islands and spits. The present modeling approach does not allow for coupling with water levels and currents. Nor does this approach include wave processes such as wave setup and swash. Wave processes at the coastline could be important for estimating flood hazard and risk especially given the increase in the offshore annual extreme wave height and number of rough days per year described herein. Further investigation into hydrodynamic-wave coupling and the quantification of potential water-level changes with climate change will provide value insights to support resource decisions.

8. Conclusions

A high-resolution SWAN (Simulating WAves Nearshore; Booij et al., 1999) wave model, forced with ERA5 winds and waves, is calibrated and validated against *in situ* offshore and nearshore wave measurements. The model includes formulations that

https://doi.org/10.5194/tc-2021-343
Preprint. Discussion started: 29 November 2021

describe wind-wave growth due to air/sea temperature differences (Le Roux, 2009) and new formulations (Rogers, 2019) to account for limited wave growth and increased energy dissipation within the Marginal Ice Zone (MIZ). The inclusion of air/sea temperature differences influenced the wind to sea drag coefficient by ±20%. Empirical ice coefficients that are typical for pancake and frazil ice resulted in the best model skill. Sensitivity analyses showed that the friction formulation of Collins (Collins-BFF; Collins, 1972) with a coefficient of 0.020 resulted in the best fit compared to observations. The model validation reveals acceptable skill in reproducing over 10,000 *in situ* observations over a 13-year time period. Overall, wave conditions along the central Beaufort Sea coast and in the shallow Foggy Island Bay are strongly modulated by the break-up and freeze-up of sea ice.

A 41-year hindcast simulation was done to estimate changes in the wave climate. Over the analyzed time period of 1979 through 2019, large changes in the ice concentration (IC) were found. In particular, the open water season has, on average, increased from just a few weeks a year in 1979 to more than 3 months (110 days) in 2019. The Mann-Kendall test reveals a statistically significant trend of decreasing IC_{50} of -1.3 and -1.7% per year for the summer and fall seasons, respectively. Over the same time period, no statistically significant trends in wind speed were found.

Model simulations show a five-fold increase of the yearly cumulative wave power over the 41-year analysis period. Median wave heights (H_{s50}) during the Fall months (September, October, November; SON) increased approximately 6% per year and has a strong negative correlation with IC_{50} of -0.71. High wave heights (H_{s90}) increased with a slightly lower rate of around 3% and show an even stronger negative correlation with IC_{50}. Wave periods tended to increase as well, albeit while maintaining a constant steepness. A counter-clockwise change in mean wave direction up to 0.39°/year was found over the analyzed time period. The months of July, August, September, October, and November account for 93% of the average yearly cumulative wave power and also have a strong negative correlation with IC.

Annual extreme wave heights were found to increase over time. Model simulations show an increase of average annual $H_{s,max}$ from 2.90 meters in 1979 to 4.62 meters in 2019. These modeling results equate to an increase of 4 cm per year or +1% per year and increases the number of rough days offshore from 1.5 to 13.1 days. These increases in the highest wave height occur due to later freeze-up in the fall. The shift in average storm date is 20 days from 1979 to 2019. Storms tend to have higher wind speeds and lower IC. For the highest waves, the offshore trends deviate from the pattern that emerges in the shallow parts of FIB. In particular, a depth-induced saturation that corresponds to γ of 0.4 show that part of the increase in energy is dissipated before reaching the shore. The importance of dissipation is also found for the wave power where at the 10-meter depth contour, the average cumulative yearly wave power is ±70% of the offshore wave power which decreases further to 25% at the 2-meter depth contour.

Code and data availability

Data produced are available on Sciencebase via the following URL https://doi.org/10.5066/P990NDMQ.

https://doi.org/10.5194/tc-2021-343
Preprint. Discussion started: 29 November 2021

Author contribution

All co-authors contributed to the initial framework and methodology. K.N. performed the simulations and analysis. The manuscript was written by K.N., while all other co-authors contributed by discussing, editing, and improving the paper.

Competing interests

The authors declare that they have no conflict of interest.

Acknowledgments

The authors thank Bjorn Robke for Figure 1. Funding for this research was provided by the U.S. Bureau of Ocean Energy Management through Cooperative Agreement M17AC00020 (UAF) and Interagency Agreement M17PG00046 (USGS) for the project titled: 'Wave and Hydrodynamic Modelling Within the Nearshore Beaufort Sea.' Additional financial support was provided by the U.S. Geological Survey Coastal Marine Hazards and Resources Program (LE, AE), and the University of Alaska (JK and PB). Any use of trade, firm, or product names is for descriptive purposes only and does not imply endorsement by the U.S. Government.

References

Aksenov, Y., Popova, E. E., Yool, A., Nurser, A. J. G., Williams, T. D., Bertino, L., & Bergh, J. (2017). On the future navigability of Arctic sea routes: High-resolution projections of the Arctic Ocean and sea ice. *Marine Policy*, *75*, 300–317. https://doi.org/10.1016/j.marpol.2015.12.027

Battjes, J. A., & Janssen, J. P. F. (1978). Energy loss and set-up due to breaking of random waves. *Proceedings 16th ICCE, Hamburg*.

Booij, N., Ris, R. C., & Holthuijsen, L. H. (1999). A third-generation wave model for coastal regions. I- Model description and validation. *Journal of Geophysical Research*, *104*, 7649–7666. https://doi.org/10.1029/98jc02622

Casas-Prat, M., Wang, X. L., & Swart, N. (2018). CMIP5-based global wave climate projections including the entire Arctic Ocean. *Ocean Modelling*, *123*(January), 66–85. https://doi.org/10.1016/j.ocemod.2017.12.003

Casas-Prat, M., & Wang, X. L. (2020). Projections of Extreme Ocean Waves in the Arctic and Potential Implications for Coastal Inundation and Erosion. *Journal of Geophysical Research: Oceans*, *125*(8). https://doi.org/10.1029/2019JC015745

Collins, C. O., & Rogers, W. E. (2017). *A Source Term for Wave Attenuation by Sea Ice in WAVEWATCH III ® : IC4*.

https://doi.org/10.5194/tc-2021-343
Preprint. Discussion started: 29 November 2021

Collins, J. I. (1972). Prediction of shallow-water spectra. *Journal of Geophysical Research (1896-1977)*, *77*(15), 2693–2707. https://doi.org/10.1029/JC077i015p02693

Curchitser, E. N., Hedstrom, K., Danielson, S., & Kasper, J. (2018). *Development of a Very High-Resolution Regional Circulation Model of Beaufort Sea Nearshore Areas*. *OCS Study BOEM 2018-018*, 81.

Dmitrenko, I., Gribanov, V. A., Volkov, D. L., Kassens, H., & Eicken, H. (1999). Impact of river discharge on the fast ice extension in the Russian Arctic shelf area. Proceedings of the 15 Th International Conference on Port and Ocean Engineering under Arctic Conditions (POAC99), Helsinki, 23-27 August, 1999, Vol. 1, 311-321.

Dunton, K. H., Reimnitz, E., & Schonberg, S. (1982). An Arctic Kelp Community in the Alaskan Beaufort Sea. *Arctic*, *35*(4), 465–484. http://www.jstor.org/stable/40509381

Erikson, L. H., Gibbs, A. E., Richmond, B. M., Storlazzi, C. D., Jones, B. M., & Ohman, K. A. (2020). Changing Storm Conditions in Response to Projected 21st Century Climate Change and the Potential Impact on an Arctic Barrier Island – Lagoon System — A Pilot Study for Arey Island and Lagoon , Eastern Arctic Alaska. *USGS Open-File Report*. https://doi.org/https://doi.org/10.3133/ofr20151193

Erikson, L. H., McCall, R. T., Rooijen, A. van, & Norris, B. (2015). Hindcast storm events in the Bering Sea for the St. Lawrence Island and Unalakleet Regions, Alaska. *USGS Open-File Report*. https://pubs.er.usgs.gov/publication/ofr20151193

Erikson, L. H., Hegermiller, C. E., Barnard, P. L., & Storlazzi, C. D. (2016). Wave Projections for United States Mainland Coasts. *US Geological Survey Pamphlet to Accompany Data Release*.

Francis, O. P., Panteleev, G. G., & Atkinson, D. E. (2011). Ocean wave conditions in the Chukchi Sea from satellite and in situ observations. *Geophysical Research Letters*, *38*(24), 1–5. https://doi.org/10.1029/2011GL049839

Frey, K. E., Moore, G. W. K., Cooper, L. W., & Grebmeier, J. M. (2015). Divergent patterns of recent sea ice cover across the Bering, Chukchi, and Beaufort seas of the Pacific Arctic Region. *Progress in Oceanography*, *136*, 32–49. https://doi.org/10.1016/j.pocean.2015.05.009

Gallaway, B. J., Britch, R. P., 1983. *Environmental summer studies (1982) for the Endicott development.* LGL Alaska Research Associates Northern Technical Services., and Sohio Alaska Petroleum Company, Fairbanks, Alaska.

Gorrell, L., Raubenheimer, B., Elgar, S., & Guza, R. T. (2011). SWAN predictions of waves observed in shallow water onshore of complex bathymetry. *Coastal Engineering*, *58*(6), 510–516. https://doi.org/10.1016/j.coastaleng.2011.01.013

Graham, R. M., Hudson, S. R., & Maturilli, M. (2019). Improved Performance of ERA5 in Arctic Gateway Relative to Four Global Atmospheric Reanalyses. *Geophysical Research Letters*, *46*(11), 6138–6147. https://doi.org/10.1029/2019GL082781

Hasselmann, K., Barnett, T. P., Bouws, E., Carlson, H., Cartwright, D. E., Enke, K., Erwing, J. A., Gienapp, H., Hasselmann, D. E., Kruseman, P., Meerburg, A., Muller, P., Ollbers, D., Richter, K., Sell, W., & Walden, H. (1973). Measurements of wind−wave growth and swell decay during the Joint North Sea Wave Project (JONSWAP), Dtsch. Hydrogr. Z. Suppl., 12, A8

Hersbach, H., Bell, B., Berrisford, P., Hirahara, S., Horányi, A., Muñoz-Sabater, J., Nicolas, J., Peubey, C., Radu, R., Schepers, D., Simmons, A., Soci, C., Abdalla, S., Abellan, X., Balsamo, G., Bechtold, P., Biavati, G., Bidlot, J., Bonavita, M., … Thépaut, J. N. (2020). The ERA5 global reanalysis. *Quarterly Journal of the Royal Meteorological Society*, *March*, 1–51. https://doi.org/10.1002/qj.3803

Kendall, M. . (1975). Rank Correlation Methods. 4th Edition, Charles Griffin, London.

Le Roux, J. P. (2009). Characteristics of developing waves as a function of atmospheric conditions, water properties, fetch and duration. *Coastal Engineering*, *56*(4), 479–483. https://doi.org/10.1016/j.coastaleng.2008.10.007

Liu, Q., Babanin, A. V., Zieger, S., Young, I. R., & Guan, C. (2016). Wind and wave climate in the Arctic Ocean as observed by altimeters. *Journal of Climate*, *29*(22), 7957–7975. https://doi.org/10.1175/JCLI-D-16-0219.1

Madsen, O. S., Poon, Y. K., & Graber, H. C. (1988). Spectral wave attenuation by bottom friction: theory. *Twenty First Coastal Eng Conf*, 492–504.

Mahoney, A., Eicken, H., Gaylord, A. G., & Shapiro, L. (2007). Alaska landfast sea ice: Links with bathymetry and atmospheric circulation. Journal of Geophysical Research: Oceans, 112(2). https://doi.org/10.1029/2006JC003559

Mahoney, A. R., Eicken, H., Gaylord, A. G., & Gens, R. (2014). Landfast sea ice extent in the Chukchi and Beaufort Seas: The annual cycle and decadal variability. *Cold Regions Science and Technology*, *103*, 41–56. https://doi.org/https://doi.org/10.1016/j.coldregions.2014.03.003

Mahoney, A. R., Hutchings, J. K., Eicken, H., & Haas, C. (2019). Changes in the Thickness and Circulation of Multiyear Ice in the Beaufort Gyre Determined From Pseudo-Lagrangian Methods from 2003–2015. Journal of Geophysical Research: Oceans, 124(8), 5618–5633. https://doi.org/10.1029/2018JC014911

Mann, H. B. (1945). Nonparametric Tests Against Trend. Econometrica, 13(3), 245. https://doi.org/10.2307/1907187

Meylan, M. H., Bennetts, L. G., & Kohout, A. L. (2014). In situ measurements and analysis of ocean waves in the Antarctic marginal ice zone. *Geophysical Research Letters*, *41*(14), 5046–5051. https://doi.org/10.1002/2014GL060809

Navarro, J., Varma, V., Riipinen, I., Seland, Ø., Kirkevåg, A., Struthers, H., Iversen, T., Hansson, H.-C., & Ekman, A. (2016). Amplification of Arctic warming by past air pollution reductions in Europe. *Nature Geoscience*, *9*. https://doi.org/10.1038/ngeo2673

Notz, D., & Community, S. (2020). Arctic Sea Ice in CMIP6. *Geophysical Research Letters*, *47*(10). https://doi.org/10.1029/2019GL086749

O'Rourke, R., Comay, L. B., Folger, P., Frittelli, J., Humphries, M., Leggett, J. A., Ramseur, J. L., Sheikh, P. A., & Upton, H. F. (2020). Changes in the Arctic: Background and issues for congress (updated). *Key Congressional Reports for September 2019: Part I*, 89–243.

Overland, J. E. (2009). Meteorology of the beaufort sea. Journal of Geophysical Research: Oceans, 114(5), 1–10. https://doi.org/10.1029/2008JC004861

635 Overland, J. E. (2016). A difficult Arctic science issue: Midlatitude weather linkages. *Polar Science*, *10*(3), 210–216. https://doi.org/10.1016/j.polar.2016.04.011

Pisaric, M. F. J., Thienpont, J. R., Kokelj, S. V., Nesbitt, H., Lantz, T. C., Solomon, S., & Smol, J. P. (2011). Impacts of a recent storm surge on an Arctic delta ecosystem examined in the context of the last millennium. *Proceedings of the National Academy of Sciences of the United States of America*, *108*(22), 8960–8965.
640 https://doi.org/10.1073/pnas.1018527108

Raghukumar, K., Chang, G., Spada, F., Jones, C., Janssen, T., & Gans, A. (2019). Performance characteristics of "spotter,"' a newly developed real-time wave measurement buoy. *Journal of Atmospheric and Oceanic Technology*, *36*(6), 1127–1141. https://doi.org/10.1175/JTECH-D-18-0151.1

Reguero, B. G., Losada, I. J., & Méndez, F. J. (2019). A recent increase in global wave power as a consequence of oceanic
645 warming. *Nature Communications*, *10*(1), 1–14. https://doi.org/10.1038/s41467-018-08066-0

Rogers, W. E., Babanin, A. V., & Wang, D. W. (2012). Observation-consistent input and white-capping dissipation in a model for wind-generated surface waves: Description and simple calculations. Journal of Atmospheric and Oceanic Technology, 29(9), 1329–1346. https://doi.org/10.1175/JTECH-D-11-00092.1

Rogers, W. E. (2019). *Implementation of Sea Ice in the Wave Model SWAN*.

650 Stopa, J. E., Ardhuin, F., & Girard-Ardhuin, F. (2016). Wave climate in the Arctic 1992-2014: Seasonality and trends. *Cryosphere*, *10*(4), 1605–1629. https://doi.org/10.5194/tc-10-1605-2016

Sen, P. K. (1968). Estimates of the Regression Coefficient Based on Kendall's Tau. Journal of the American Statistical Association, 63(324), 1379–1389. https://doi.org/10.1080/01621459.1968.10480934

Stroeve, J., & Notz, D. (2018). Changing state of Arctic sea ice across all seasons. *Environmental Research Letters*, *13*(10).
655 https://doi.org/10.1088/1748-9326/aade56

Thomson, J., Fan, Y., Stammerjohn, S., Stopa, J., Rogers, W. E., Girard-Ardhuin, F., Ardhuin, F., Shen, H., Perrie, W., Shen, H., Ackley, S., Babanin, A., Liu, Q., Guest, P., Maksym, T., Wadhams, P., Fairall, C., Persson, O., Doble, M., … Bidlot, J. R. (2016). Emerging trends in the sea state of the Beaufort and Chukchi seas. *Ocean Modelling*, *105*, 1–12. https://doi.org/10.1016/j.ocemod.2016.02.009

660 Thomson, J., & Rogers, W. E. (2014). Swell and sea in the emerging Arctic Ocean. *Geophysical Research Letters*, *41*(9), 3136–3140. https://doi.org/10.1002/2014GL059983

Van Der Westhuysen, A. J. (2010). Modeling of depth-induced wave breaking under finite depth wave growth conditions. *Journal of Geophysical Research: Oceans*, *115*(1), 1–19. https://doi.org/10.1029/2009JC005433

Wang, M., & Overland, J. (2015). Projected Future Duration of the Sea-Ice-Free Season in the Alaskan Arctic. *Progress in*
665 *Oceanography*. https://doi.org/10.1016/j.pocean.2015.01.001

Wang, X. L., Semedo, A., Dobrynin, M., & Hemer, M. A. (2016). *Report of the 2016 WCRP-JCOMM Coordinated Ocean Wave Climate Project Workshop, Vienna, April 19, 2016. JCOMM Technical Report 89.*

https://doi.org/10.5194/tc-2021-343
Preprint. Discussion started: 29 November 2021

Wang, X., & Swail, V. (2001). Changes of Extreme Wave Heights in Northern Hemisphere Oceans and Related Atmospheric Circulation Regimes. *Journal of Climate*, *14*, 2204–2221. https://doi.org/10.1175/1520-0442(2001)01460;2204:coewhi62;2.0.co;2

Zanowski, H., Jahn, A., & Holland, M. M. (2021). Arctic Ocean Freshwater in CMIP6 Ensembles: Declining Sea Ice, Increasing Ocean Storage, and Export. *Journal of Geophysical Research: Oceans*, *126*(4). https://doi.org/10.1029/2020JC016930